

Hierarchical MPC for Robust Eco-Cooling of Connected and Automated Vehicles and Its Application to Electric Vehicle Battery Thermal Management

Mohammad Reza Amini¹, Ilya Kolmanovsky², *Fellow, IEEE*, and Jing Sun¹, *Fellow, IEEE*

Abstract—Connected and autonomous vehicles (CAVs) have situational awareness that can be exploited for optimal power and thermal management. In this article, we develop a hierarchical model predictive control (H-MPC) strategy for eco-cooling of CAVs, which reduces energy consumption through real-time prediction and multi-timescale and multi-layer optimization. The application of the proposed H-MPC is studied for battery thermal and energy management of an electric vehicle (EV). Our H-MPC approach addresses the uncertainty in the long-term preview of the vehicle speed through robust constraint handling to prevent constraint violation. The simulation results show that compared with a conventional battery thermal management (BTM) strategy, the proposed robust H-MPC saves the battery energy by up to 5.4% under the uncertainties in the long-term vehicle speed predictions in an urban CAV operation scenario.

Index Terms—Connected and automated vehicles (CAVs), hierarchical model predictive control (H-MPC), thermal management.

NOMENCLATURE

C_{nom}	Battery nominal capacity [Wh].
$C_{\text{th, bat}}$	Battery heat capacity [J/kg · K].
H_s	Scheduling layer prediction horizon [step].
H_p	Piloting layer prediction horizon [step].
I_{bat}	Battery current [A].
m	Vehicle mass [kg].
m_{bat}	Battery mass [kg].
P_{BTM}	BTM power [W].
P_{trac}	Traction power [W].
\dot{Q}	Battery cooling/heating flow rate [W].
R_{bat}	Battery resistance [Ω].
SOC	Battery state-of-charge [–].

T_{bat}	Battery pack temperature [$^{\circ}\text{C}$].
T	Sampling time [s].
T_s	Sampling time of the scheduling layer [s].
T_p	Sampling time of the piloting layer [s].
U_{bat}	Battery voltage [V].
V_{veh}	Vehicle speed [m/s].
$\epsilon, \zeta, \sigma, \text{ and } \zeta$	Slack variables [$^{\circ}\text{C}$].

ACRONYMS

A/C	Air conditioning.
BTM	Battery thermal management.
CAV	Connected and automated vehicle.
CT	Constraint tightening.
HEV/EV	Hybrid electric vehicle/electric vehicle.
H-MPC	Hierarchical model predictive control.
S-MPC	Single-layer model predictive control.
UDDS	Urban dynamometer driving schedule.
V2I/V2V	Vehicle-to-infrastructure/vehicle.

I. INTRODUCTION

CAVs equipped with advanced sensors for perception and localization are expected to provide enhanced safety and improved mobility [1], and there is a growing interest in fuel/energy efficiency improvements possible with CAVs [2], [3]. Most of the recent CAV-related studies, such as on eco-driving and on platooning, has been focused on reducing traction power-related losses (see [2], [3] and the references therein). Relatively little has been reported, on the other hand, on efficient thermal management (i.e., eco-driving) of CAVs exploiting information accessible through V2V and V2I communications [4], [5].

Thermal management of electrified vehicles, including HEVs and pure EVs, is a significant factor in the overall vehicle energy consumption optimization. For EVs with relatively large battery packs, the need to cool the battery in hot summer days takes a substantial amount of energy and reduces the driving range [6], [7]. Moreover, since the power for cooling the battery pack is delivered by the battery itself, the operation of the BTM system directly interacts with other power loads, such as the traction power, forming intricate feedback loops. Therefore, optimization of BTM system is essential for improving the overall vehicle energy efficiency.

Manuscript received July 3, 2019; revised February 2, 2020; accepted February 12, 2020. Manuscript received in final form February 17, 2020. This work was supported by the United States Department of Energy (DOE) through the Advanced Research Projects Agency-Energy (ARPA-E) NEXTCAR Program under Award DE-AR0000797. Recommended by Associate Editor L. Fagiano. (*Corresponding author: Mohammad Reza Amini.*)

Mohammad Reza Amini and Jing Sun are with the Department of Naval Architecture and Marine Engineering, University of Michigan, Ann Arbor, MI 48109 USA (e-mail: mamini@umich.edu; jingsun@umich.edu).

Ilya Kolmanovsky is with the Department of Aerospace Engineering, University of Michigan, Ann Arbor, MI 48109 USA (e-mail: ilya@umich.edu).

Color versions of one or more of the figures in this article are available online at <http://ieeexplore.ieee.org>.

Digital Object Identifier 10.1109/TCST.2020.2975464

An overview of the literature on optimization of BTM in EVs is provided in [8]. Pontryagin's maximum principle is used in [6] to optimize the battery thermal and energy management dynamics. In [9], dynamic programming (DP) is exploited to find the global optimal solution to the BTM optimization problem. Bauer *et al.* [6] and Masoudi *et al.* [9] have shown the benefits of using optimization in minimizing the required cooling power to maintain the battery temperature within the optimal operating range. However, their approaches are predicated on the assumption that the whole driving cycle is known *a priori*. Furthermore, despite the reported energy savings, the dependencies of the BTM strategy on the driving cycle, the coupling between the thermal and traction loads on the battery, and the sensitivity of the BTM performance to the accuracy of the future vehicle speed and the traffic event predictions have not been fully evaluated.

There are several challenges in the development of a real-time optimization strategy for BTM in electrified CAVs that are associated with the following special characteristics:

- 1) *Large Thermal Inertia*: A long time horizon is required for the optimization of the battery thermal response due to the slow thermal dynamics, leading to an increase in the computational footprint to an extent that can make it infeasible for real-time implementation.
- 2) *Coupling Between Traction and Thermal Loads*: For EVs, the electric battery is the only power source to meet both traction and thermal management demands. The maximum heat generation within the battery occurs during high-acceleration and high-deceleration periods when the traction power demand is high.
- 3) *Sensitivity to Traffic Forecast Uncertainty*: While the vehicle speed profile can be accurately predicted using V2V/V2I information over a short time horizon [10], [11], its accurate longer term prediction is difficult.

To address the challenges in designing a real-time controller for eco-cooling of connected EVs, a hierarchical two-layer model predictive control (MPC) formulation for battery thermal and energy management optimization is presented in this article. The approach that we are taking is built upon our preliminary work [12] and is inspired—in part—by the recent literature on multilayer optimization and prediction for systems with multiple timescales, including microgrids [13], power flow [14], building energy management [15], and automotive climate control [16] systems. The proposed H-MPC cools the battery pack by keeping its temperature within a prescribed range based on traffic conditions and vehicle power demand. Assuming that traffic conditions can be predicted either onboard of a CAV or by CAV supporting infrastructure, the proposed H-MPC exploits the timescale separation between the power and thermal responses to shift the BTM load, thereby improving the overall vehicle energy efficiency. Compared with [12], this article significantly expands the baseline H-MPC by: 1) exploiting the concept of eco-cooling enabled by thermal load shift; 2) investigating the impact of extending the prediction horizon and long-term vehicle speed prediction uncertainty on the BTM and vehicle energy consumption, as well as the computational footprint

through extensive simulations; and 3) developing a new robust H-MPC strategy.

The contribution of this article is fourfold. First, the energy-saving potential of the MPC-based BTM system in EVs is exploited by utilizing the vehicle speed preview inferred from the traffic flow information over a long prediction horizon. Second, a two-layer MPC framework is developed to reduce the computation footprint and to account for different timescales of prediction and control of power and thermal systems. Third, the impact of accuracy in vehicle speed prediction on BTM performance is explored and quantified. Fourth, two CT algorithms are developed and incorporated into the H-MPC to improve the robustness against the demand preview uncertainty.

This article is organized as follows. In Section II, control-oriented models for EV battery thermal and electrical subsystems are presented. In Section III, a single-layer economic MPC-based BTM strategy is developed, which serves as the baseline MPC for performance evaluation of the proposed H-MPC. The impact of prediction horizon length on the BTM performance and the importance of thermal load shifting for eco-cooling are also discussed in this section. Moreover, the sensitivity of the MPC-based BTM to the uncertainty in the future vehicle speed prediction is explored. In Section IV, an H-MPC framework for BTM with vehicle speed prediction incorporated over accurate, but short, and long, but uncertain prediction horizons is proposed. CT approaches for robust H-MPC are developed in Section V. Next, different aspects of the baseline and robust H-MPC performances for BTM will be discussed in detail in Section VI. Finally, concluding remarks are presented in Section VII.

II. BATTERY THERMAL AND ELECTRICAL MODELS

To implement an MPC for BTM system, both electrical and thermal characteristics of the battery have to be captured by the prediction model. The thermal sub-model approximates the battery pack as a lumped mass (m_{bat}) with heat capacity $C_{\text{th,bat}}$ and has the form [6]

$$\dot{T}_{\text{bat}}(t) = \frac{1}{m_{\text{bat}}C_{\text{th,bat}}}(I_{\text{bat}}^2 R_{\text{bat}} + \dot{Q} + \dot{Q}_a) \quad (1)$$

where T_{bat} , I_{bat} , and R_{bat} are the battery temperature, current, and internal resistance, respectively. The heat exchange with ambient is denoted by \dot{Q}_a . $\dot{Q} \leq 0$ is the heat flow rate for cooling the battery, which is treated as the input to the battery thermal model in this article. In practice, \dot{Q} is provided through a combination of air- and liquid-cooling loops in EVs [17]. The liquid cooling is provided by an electric A/C compressor and a coolant loop. The air cooling regulates the battery temperature by blowing the passenger compartment air into the battery pack using a fixed or a variable-speed fan. Since the compartment air is cooled by the A/C compressor, the battery air cooling loop is also coupled to the A/C system. The schematic of BTM system in an EV with air- and liquid-cooling loops is shown in Fig. 1.

The electric system sub-model of the battery includes the battery voltage (U_{bat}), which can be expressed as a function

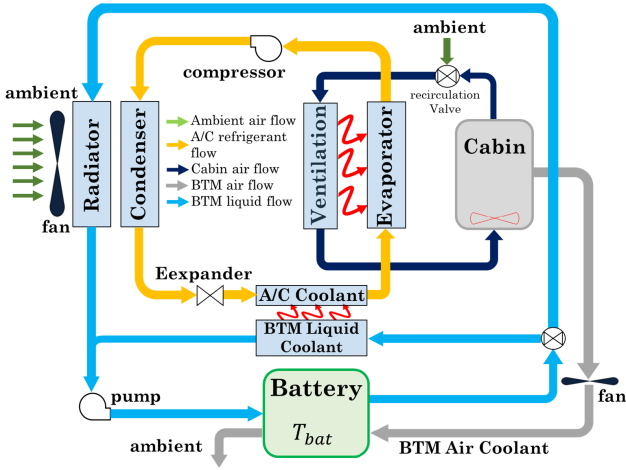


Fig. 1. Schematic of the BTM system in an EV with A/C refrigerant and air- and liquid-cooling loops. The generated heat within the battery, depending on its rate, is rejected (\dot{Q}) through a combination of air- and liquid-coolant loops.

of the open-circuit voltage (U_{oc}), internal resistance R_{bat} , and current drawn I_{bat} , as follows:

$$U_{bat} = U_{oc} - I_{bat}R_{bat}. \quad (2)$$

In (2), U_{oc} and R_{bat} are functions of the battery state-of-charge (SOC) and T_{bat} . The battery current can be written as a function of the total demanded power as follows:

$$I_{bat} = (P_{trac} + P_{BTM})/U_{bat} \quad (3)$$

where P_{trac} is the demanded traction power and P_{BTM} is the power required to provide \dot{Q} for the BTM system. Equation (3) assumes that P_{trac} and P_{BTM} are the main power loads on the battery, and other auxiliary loads on the battery are neglected. By substituting U_{bat} into (2) by $(P_{trac} + P_{BTM})/I_{bat}$ based on (3), I_{bat} can be rewritten as

$$I_{bat}(t) = \frac{U_{oc} - \sqrt{U_{oc}^2 - 4R_{bat}(P_{trac} + P_{BTM})}}{2R_{bat}}. \quad (4)$$

Using (4), (1) becomes

$$\dot{T}_{bat}(t) = \frac{(U_{oc} - \sqrt{U_{oc}^2 - 4R_{bat}(P_{trac} + P_{BTM})})^2}{4R_{bat}} + \dot{Q} + \dot{Q}_a. \quad (5)$$

Moreover, the evolution of SOC is governed by

$$\dot{\text{SOC}}(t) = -\frac{I_{bat}}{C_{nom}} \quad (6)$$

where C_{nom} is the nominal capacity of the battery. The demanded traction power can be estimated as [6]

$$P_{trac} = \begin{cases} \frac{V_{veh}(F_r + F_a + m\dot{V}_{veh})}{\eta}, & \text{propelling} \\ V_{veh}(F_r + F_a + m\dot{V}_{veh})\eta, & \text{braking} \end{cases} \quad (7)$$

where V_{veh} and m are the vehicle speed and mass, $\eta = \eta(\tau, \omega)$ is the traction system efficiency, which is a function of the torque (τ) and the rotation speed (ω) of the electric motor, and it is calculated by using a lookup table, and F_r and F_a are

rolling and aerodynamic resistances, respectively, calculated as follows:

$$F_r = C_r mg \quad (8)$$

$$F_a = 0.5\rho A_f C_d V_{veh}^2. \quad (9)$$

In (8) and (9), C_r and C_d are the rolling resistance and aerodynamic drag coefficients, A_f is the vehicle frontal area, and ρ is the air density. In this article, we assume that all the brakings can be accommodated through electric brakes; thus, we have not considered the friction braking in the vehicle dynamic model (7). Note that the regenerative braking, unlike the friction braking, directly affects the battery thermal response during the battery charging. In the absence of the friction braking, the vehicle model considered in this article represents the maximum thermal load on the battery due to regenerative braking. This assumption is consistent with the practice, where the use of friction brakes is minimized to improve energy efficiency and reduce wear.

The BTM cooling power P_{BTM} is modeled as a linear function of the rejected heat flow rate \dot{Q} from battery [6]

$$P_{BTM}(\dot{Q}) = a_c \dot{Q}, \quad \dot{Q} \leq 0, \quad a_c < 0 \quad (10)$$

where a_c is a constant. We assume that the maximum P_{BTM} is limited at 1.5 kW, which is associated with the maximum heat rejection rate (\dot{Q}_{max}) of 500 W, i.e., $a_c = 3$. This value of a_c is selected based on the SAE J3073 standard [18]. The parameters of the battery and vehicle longitudinal dynamics are adopted from the Autonomie [19] software library for an EV. A virtual testbed to carry out simulations has been implemented based on the high-fidelity thermal and electrical models of the battery, along with R_{bat} , U_{oc} , and η lookup tables extracted from Autonomie.

Remark 1: As we are optimizing the BTM system operation at the system level, the details of the underlying electric/fluid/thermal systems and their controllers (shown in Fig. 1) are not considered. The delivery of \dot{Q} is performed by lower level controllers with multiple actuators (e.g., compressor, fan, and pump). Similarly, while the electric/fluid/thermal hysteresis is an important characteristic for the open-loop controller dynamics, at the system level, it is assumed that this hysteresis is compensated by the components controllers. This approach is consistent with the number of other studies (see [6], [9]).

Remark 2: While the linear relationship considered in (10) may be oversimplifying the underlying thermal loops, it is adequate for the purpose of demonstrating approaches to optimizing the thermal load of BTM system (\dot{Q}).

III. S-MPC

In this section, an economic S-MPC is developed to minimize the required battery cooling power and maintain the battery temperature within the desired operating range. This approach differs from the traditional BTM that attempts to maintain the battery temperature at a specified level, without considering the traffic information.

In order to formulate the S-MPC, first, the thermal and electric models [see (6) and (5)] are discretized by applying

the Euler forward method to obtain

$$\text{SOC}(k+1) = f_{\text{SOC}}(k) = \text{SOC}(k) - T \left(\frac{U_{\text{oc}}(k) - \sqrt{U_{\text{oc}}^2(k) - 4R_{\text{bat}}(k)(P_{\text{trac}}(k) + P_{\text{BTM}}(k))}}{2C_{\text{nom}}R_{\text{bat}}(k)} \right) \quad (11)$$

$$T_{\text{bat}}(k+1) = f_{T_{\text{bat}}}(k) = T_{\text{bat}}(k) + T \left(\frac{\frac{(U_{\text{oc}}(k) - \sqrt{U_{\text{oc}}^2(k) - 4R_{\text{bat}}(k)(P_{\text{trac}}(k) + P_{\text{BTM}}(k))})^2}{4R_{\text{bat}}(k)} + \dot{Q}(k) + \dot{Q}_a}{m_{\text{bat}}C_{\text{th,bat}}} \right) \quad (12)$$

where T is the sampling period between the control updates. Over the prediction horizon of the MPC-based BTM controller, we assume a constant \dot{Q}_a at the constant ambient temperature of $T_a = 30^\circ\text{C}$. \dot{Q}_a is updated based on the feedback from the high-fidelity model at next time step. Our S-MPC uses an economical cost function that is defined over a finite-time horizon (N) and is minimized with respect to \dot{Q} sequences

$$\begin{aligned} \min_{\dot{Q}(\cdot|k), \sigma(\cdot|k)} \sum_{i=0}^N P_{\text{BTM}}(i|k) + \gamma_1 \sigma(i|k) \\ \text{s.t. } T_{\text{bat}}(i+1|k) = f_{T_{\text{bat}}}(i|k), \quad i = 0:N \\ \text{SOC}(i+1|k) = f_{\text{SOC}}(i|k), \quad i = 0:N \\ T_{\text{bat}}^{\text{LL}} \leq T_{\text{bat}}(i|k) \leq T_{\text{bat}}^{\text{UL}} + \sigma(i|k), \quad i = 0:N \\ 0.3 \leq \text{SOC}(i|k) \leq 0.9, \quad i = 0:N \\ -\dot{Q}_{\text{max}} \leq \dot{Q}(i|k) \leq 0, \quad i = 0:N-1 \\ 0 \leq \sigma(i|k), \quad i = 0:N-1 \\ T_{\text{bat}}(0|k) = T_{\text{bat}}(k), \quad \text{SOC}(0|k) = \text{SOC}(k) \end{aligned} \quad (13)$$

where $(i|k)$ designates the prediction for the time instant $k+iT$ made at the time instant k . In (13), $T_{\text{bat}}^{\text{UL}}$ and $T_{\text{bat}}^{\text{LL}}$ are the upper and lower limits of the battery operating temperature, which are set to 40°C and 20°C [20], respectively. Since the battery temperature upper limit $T_{\text{bat}}^{\text{UL}}$ is often considered to be a soft constraint [6], [20], temporary violations of this constraints are allowed by introducing slack optimization variable σ in the MPC stage cost and T_{bat} constraint. The weighting factor for the slack variable in the state cost is constant ($\gamma_1 = 10^7$). If the battery temperature remains above this limit for a prolonged period of time, however, it could be detrimental to the battery state-of-health [7]. Note that \dot{Q} is always nonpositive for battery cooling scenario. In this article, simulations and the analysis of simulation results are done for zero-grade road. The optimization problem is solved at every time step, and then, the horizon is shifted by one step (T); only the current control is commanded to the system ($\dot{Q}(k) = \dot{Q}(0|k)$). The closed-loop simulations with S-MPC controller are carried out on a desktop computer, with an Intel Core i7 at 2.60 GHz processor, in MATLAB/SIMULINK using YALMIP [21] for formulating the optimization problem and Interior Point OPTimizer (IPOPT) [22] for solving the optimization problem numerically.

Remark 3: Due to the nonlinearity in the battery SOC (f_{SOC}) and T_{bat} ($f_{T_{\text{bat}}}$) models, the optimization problems considered and solved in this article [e.g., (13)] are nonconvex. We note

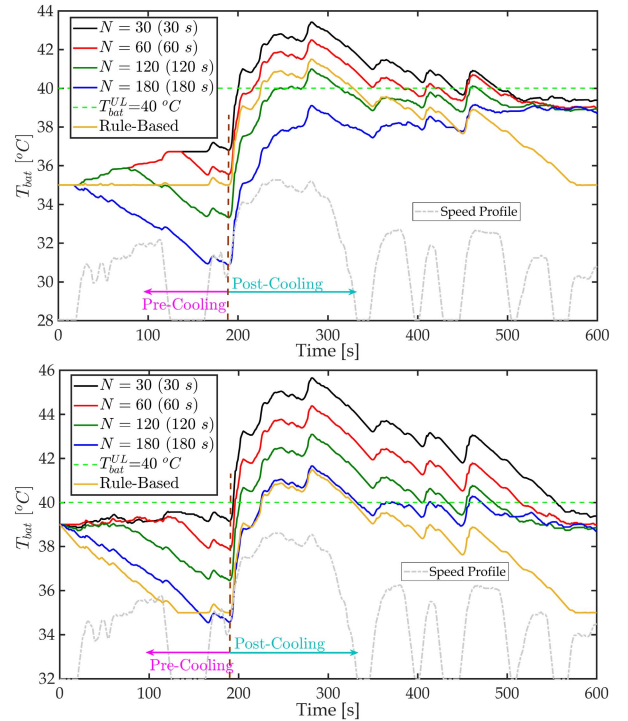


Fig. 2. Time histories of the battery temperature with the S-MPC for different prediction horizons and with the rule-based controller for BTM for $T_{\text{bat}}(0) = 35^\circ\text{C}$ (top) and $T_{\text{bat}}(0) = 39^\circ\text{C}$ (bottom) over the UDDS ($T = 1$ s).

that there are effective techniques that can be leveraged to facilitate the nonlinear optimization by using convex approximation of the battery system [23], [24], considering them falls outside the scope of this article.

A. Impact of Prediction Horizon on the S-MPC Performance

Fig. 2 illustrates the sensitivity of the S-MPC (13) to the prediction horizon length for initial battery temperatures of $T_{\text{bat}}(0) = 35^\circ\text{C}$ (top) and 39°C (bottom). The initial value for the battery SOC is set to $\text{SOC}(0) = 0.85$ (85%) for all the simulated cases. The simulated driving cycle is the first 600 s of the Environmental Protection Agency (EPA) UDDS, which includes both city and highway (with high traction power demand) driving scenarios with multiple stops. It is assumed that the vehicle velocity over the whole driving cycle is known *a priori* to the S-MPC; this assumption will be relaxed in Section III-C.

In addition to MPC-based BTM results, Fig. 2 shows the results of implementing a rule-based controller for BTM as the benchmark case. This rule-based controller has a simple logic which tries to maintain the battery temperature at a constant set-point ($T_{\text{bat}}^{\text{s.p.}}$) regardless of the vehicle speed and traction power demand preview. The command of the rule-based BTM controller is calculated as follows:

$$\dot{Q} = \begin{cases} -\dot{Q}_{\text{max}}, & \text{if } T_{\text{bat}} > T_{\text{bat}}^{\text{s.p.}} \\ 0, & \text{if } T_{\text{bat}} \leq T_{\text{bat}}^{\text{s.p.}} \end{cases} \quad (14)$$

For the rule-based controller, the conventional approach to reduce the battery temperature limit violations is to set the set-point ($T_{\text{bat}}^{\text{s.p.}}$) in the middle of the optimal temperature range

of the battery operation. Since the battery temperature can change rapidly during aggressive vehicle accelerations and the BTM has limited bandwidth to respond, the set-point $T_{\text{bat}}^{s.p.}$ is usually selected well below the upper limit of the optimum operation range. For instance, in the simulations of the rule-based controller, $T_{\text{bat}}^{s.p.} = 35^\circ\text{C}$ is used. As will be shown later, this conservative rule-based approach may lead to considerable extra energy consumed for battery cooling.

As can be observed from Fig. 2, increasing the prediction horizon N from 30 (30 s) to 180 (180 s) leads to a significant change in the battery temperature behavior. When the prediction horizon is relatively short (60 or less), S-MPC minimizes the BTM power consumption within the short window; consequently, it leads the battery temperature to the upper temperature limit ($T_{\text{bat}}^{\text{UL}}$). When the vehicle enters the highway segment part of the trip around $t = 180$ s, the demanded traction power rises suddenly, and, as a result, S-MPC is not able to maintain the battery temperature below the specified limit of 40°C . Note that for $N = 30$, the controller does not have enough lead time to take mitigating actions to prevent constraint violation caused by sudden increase in the traction power, and the battery temperature can rise to almost 46°C for the initial battery temperature equal to 39°C . It is also noted that for $T_{\text{bat}}(0) = 39^\circ\text{C}$ and $N = 30$, the battery temperature remains above the upper limit for a prolonged period of time, including after the highway driving segment is over, which, as discussed earlier, is not preferred.

Frequent violation of $T_{\text{bat}}^{\text{UL}}$ is the price paid for allowing the battery temperature to operate near its limit to minimize the BTM power consumption with a relatively short prediction horizon. On the other hand, Fig. 2 shows that as the prediction horizon N is being extended, S-MPC takes proactive actions to reduce the temperature before the vehicle enters the highway segment and the heating load increases, therefore significantly reducing the time for the battery to stay in overtemperature condition. When $T_{\text{bat}}(0) = 35^\circ\text{C}$, by increasing the prediction horizon from 30 to 180, S-MPC decreases T_{bat} from the beginning, which eventually results in zero constraint violation. A similar behavior is observed for $T_{\text{bat}}(0) = 39^\circ\text{C}$ with different prediction horizons. With $T_{\text{bat}}(0) = 39^\circ\text{C}$, battery temperature constraint violation cannot be avoided due to higher initial battery temperature and limited capacity of the BTM system. It should be noted that depending on the battery sizing and configuration, the vehicle dynamics, and the BTM system structure, the rate of the change in the battery temperature could vary. Despite these variations, the observation from Fig. 2 is generalizable in the sense that there are benefits of extending the prediction horizon and incorporating more information from the “predicted future” to enhance the battery temperature constraint enforcement using an economic MPC formulation [e.g., S-MPC (13)].

As illustrated in Fig. 2, depending on the prediction/preview horizon, S-MPC results in either.

- 1) BTM with “Post-Cooling” if the horizon is short.
- 2) BTM with “Pre-Cooling” if the horizon is longer.

The “post-cooling” is essentially a reactive strategy that cools the battery after the generated heat within the battery

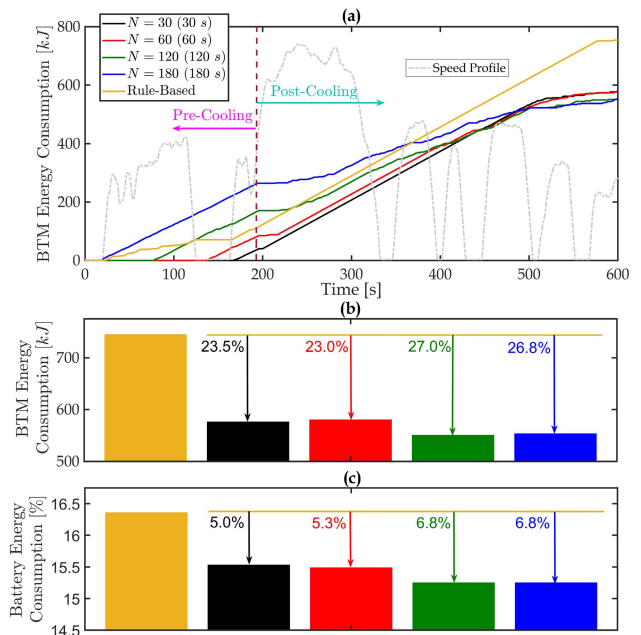


Fig. 3. Impact of the prediction horizon for S-MPC. (a) BTM energy consumption. (b) BTM energy consumption compared with rule-based controller. (c) Overall battery energy consumption for $T_{\text{bat}}(0) = 35^\circ\text{C}$ and $T = 1$ s.

drives the temperature to/above the upper operating limit $T_{\text{bat}}^{\text{UL}}$. As shown in Fig. 2, the “post-cooling” approach is not able to prevent the temperature constraint violations and, as shown in Figs. 3 and 4, does not lead to smallest BTM power consumption even though it operates the battery near its upper temperature limit and with lowest energy consumption before the acceleration event. By comparing the closed-loop responses with S-MPC for $N = 30$ and S-MPC for $N = 180$, it can be observed that the longer horizon S-MPC pre-cools the battery when the traction load is not considerable (i.e., before $t = 180$ s), and then, it reduces the BTM energy consumption rate after $t = 180$ s when the demanded traction power on the battery is higher. Since the generated heat within the battery is higher when power draw from the battery is higher, reducing cooling load when the traction load is higher translates into overall reduced energy consumption. Note that the S-MPC with long horizon pre-cools the battery temperature within the optimum temperature range (e.g., 20°C – 40°C), where the variations of R_{bat} and U_{oc} , as a function of T_{bat} , are not considerable [25].

Compared with the rule-based controller (14), Fig. 3 shows the benefits of the economic S-MPC in saving the energy consumed for cooling the battery. The percentage of the battery energy consumption in Fig. 3(c) is calculated with respect to the change in the battery SOC at the end of the driving cycle ($\text{SOC}(k_f)$) compared with the initial state of charge ($\text{SOC}(0)$)

$$\text{Battery Energy Consumption} = \frac{\text{SOC}(0) - \text{SOC}(k_f)}{\text{SOC}(0)} \times 100. \quad (15)$$

Depending on the prediction horizon length, S-MPC reduces the energy consumed for BTM [see Fig. 3(b)] and the overall battery energy consumption [see Fig. 3(c)] by 23%–27.0%

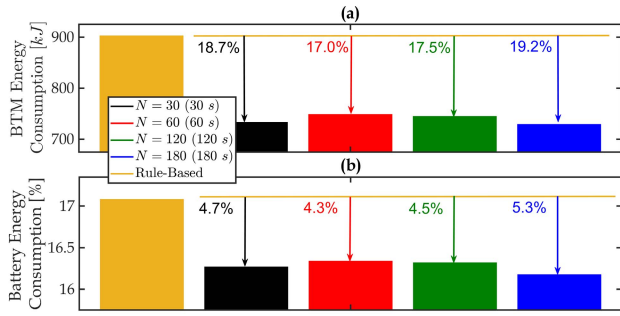


Fig. 4. Impact of the prediction horizon for S-MPC. (a) BTM energy consumption compared with a rule-based controller. (b) Overall battery energy consumption for $T_{\text{bat}}(0) = 39$ °C and $T = 1$ s.

and 5%–6.8%, respectively, compared with the rule-based controller. It can be seen that by increasing N from 30 to 180, first, the total energy consumed for BTM slightly increases, and then, as N increases, it decreases. For the overall battery energy consumption, Fig. 3(c) shows the drop in the consumed energy as the prediction horizon is extended. At $N = 180$, S-MPC improves the overall battery energy consumption by 6.8% compared with the rule-based controller. Note that despite the impact of the BTM system on vehicle energy consumption, any changes in BTM power consumption do not necessarily translate linearly to the power consumption at the vehicle level. As an example, Fig. 3(b) and (c) show that when N is increased from 30 to 60, the BTM energy consumption slightly increases, while the overall battery energy consumption decreases. This observation is investigated in detail in Section III-B.

Similar BTM performance improvements are observed for $T_{\text{bat}}(0) = 39$ °C, as shown in Fig. 4. The economic S-MPC reduces the energy consumed for BTM by 17%–19.2% compared with the rule-based controller. This reduction in the BTM energy consumption leads to 4.3%–5.3% decrease in the overall battery energy consumption, depending on N . The extensive simulation results showed that extending N to beyond 180 has no significant impact on the BTM performance.

B. Battery Eco-Cooling Enabled by Thermal Load Shift

While the results shown in Figs. 3 and 4 are for UDDS driving cycle, similar battery energy consumption reduction benefits of the battery pre-cooling strategy are expected for other urban driving cycles that consist of city driving segments with moderate speeds and frequent stops and of highway driving segments with higher speeds. For such urban driving cycles, when the prediction horizon N becomes sufficiently large, the S-MPC pre-cools the battery and shifts the BTM power demand from the highway driving segment to the city driving part where the traction power demand is generally lower. The concept of thermal load shift is illustrated in Fig. 5. Note also that the optimization over the longer horizon reduces the propensity to the battery constraint violation. The energy-efficient BTM achieved via pre-cooling and long-horizon optimization by incorporating the traffic

preview information is referred to as “eco-cooling” in the remainder of this article. Fig. 6 summarizes and illustrates the battery cooling concept as a function of the prediction horizon length with BTM energy consumption and battery temperature constraint violations being the performance indices.

Remark 4: While, in this article, we only consider UDDS driving cycle to illustrate MPC-based solution for BTM in EVs, we have investigated the MPC-based power and thermal management (PTM) of CAVs (e.g., climate control, engine, and after treatment cooptimization) over different urban driving cycles in our previous works, including New York City Cycle [12], New European Driving Cycle [26], and real-world city driving cycles in Ann Arbor, MI, USA [5]. Despite the special characteristics of each of these PTM problems (i.e., constraints, sensitivity to the length of the prediction horizon, and speed prediction uncertainty), our studies have confirmed the benefits of incorporating traffic preview to achieve efficient PTM.

C. Sensitivity of S-MPC to Accuracy of the Speed Preview

It was shown in Section III-A that the information about future driving conditions, in particular, the vehicle speed profile over a long horizon, can facilitate the design of an energy-efficient BTM system. However, there are two impediments to the implementation of S-MPC over a long horizon.

- 1) The accuracy of the vehicle speed preview over a longer horizon cannot be guaranteed.
- 2) It is computationally demanding.

While the vehicle speed profile can be accurately estimated using traffic and infrastructure information (V2I/V2X) over a short horizon [11], [27], its prediction over an extended horizon may be inaccurate, and this can degrade MPC/BTM performance.

We note that long-term forecasts of future vehicle speed needed by our control algorithms can be informed by the average traffic flow velocity (V_{flow}) following the approach proposed in [27]. In [27], the traffic flow data are extracted from a traffic monitoring system described in [28] based on GPS-enabled smartphones. This system exploits the extensive coverage of the cellular network, GPS-based position and velocity measurements, and the communication infrastructure of cellphones. Here, the traffic flow speed is calculated according to the moving average of the recorded speed trajectories of 100 vehicles traveling following the same route as the ego-vehicle (driving with the actual driving cycle speed) over a moving time window of 180 s. To this end, first, we make several assumptions. Specifically, we assume that before the start of the ego-vehicle trip with a known route, the historic data of another 100 vehicles traveling on the same route are available. These historic data, while different than that of the ego-vehicle, are representative of the traffic pattern. It is assumed all the vehicles stay on the same route (i.e., they enter the corridor at the same point in space, as well as exiting the corridor at the same point—but different than the entrance point. Note that the exiting time (total travel time) could be different as these vehicles travel at different speeds). Furthermore, we assume no vehicle, including the ego-vehicle, is driving outside of normal speed limits. These assumptions

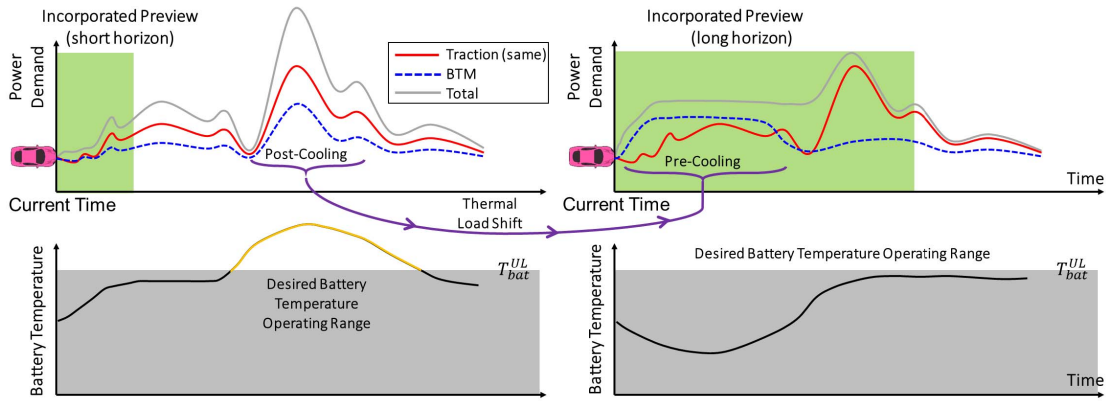


Fig. 5. Concept of thermal load shift for energy-efficient battery cooling.

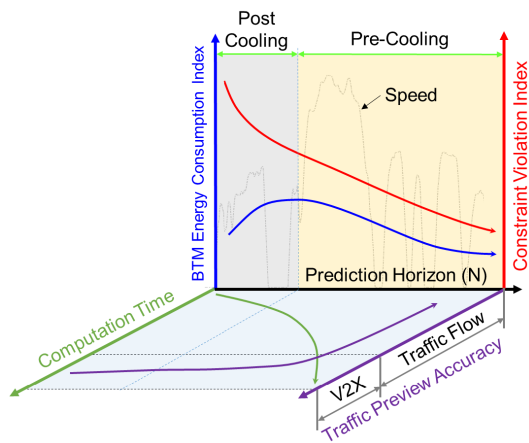


Fig. 6. Conceptual schematic of the BTM performance and energy consumption sensitivity to prediction horizon length, and associated prediction accuracy and computational complexity tradeoffs for a generic urban cycle.

are made to simplify the exposition. Next, these historic data are used to calculate a moving average that is considered as the long-term preview for the ego-vehicle.

With the above-mentioned approach, it is possible to build a dynamic map of average traffic velocity over a long horizon. The traffic flow data are assumed to be collected, analyzed, and updated by a central/cloud server in real-time, and they are available to the vehicle control system at no extra computational cost. Fig. 7 illustrates the concept of the average traffic flow speed trajectory (gray band) and compares it against the actual speed profile (blue line).

In order to assess the robustness of S-MPC in (13) to vehicle speed preview uncertainty, three cases are considered.

- 1) *Case I*: The preview of vehicle speed over the prediction horizon is exact and updated, along with the control action, at the nominal sampling period of $T = 1$ s.
- 2) *Case II*: The preview of vehicle speed over the prediction horizon is exact and updated, along with the control action, at the slower sampling period of $T = 5$ s.
- 3) *Case III*: The preview of vehicle speed over the prediction horizon is not accurate and is based on the average traffic flow speed (see Fig. 7); this and the control action are updated at the nominal sampling period of $T = 1$ s.

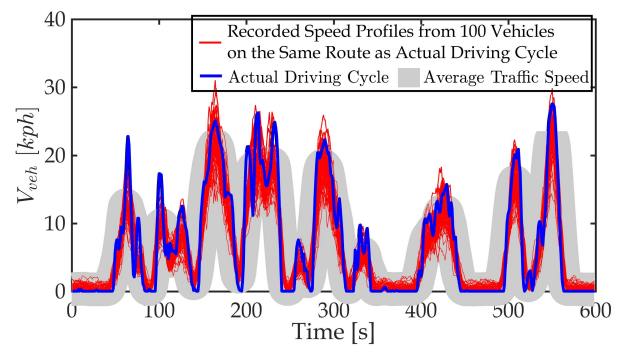


Fig. 7. Concept of average traffic flow speed estimate versus the actual speed over a driving cycle.

These three cases have been simulated for different prediction horizons, and the results are summarized in Fig. 8 in terms of battery energy consumption [see Fig. 8(a)], average computation time per iteration and execution [see Fig. 8(b)], and battery temperature constraint violation [see Fig. 8(c)].

The battery energy consumption results from Fig. 3(c) at $T_{bat}(0) = 35$ °C are repeated in Fig. 8(a) as Case I. With the exact vehicle speed preview, when the update rate is increased from $T = 1$ to 5 s (Case II), Fig. 8(a) shows that the battery energy consumption increases for $N = 120$ s (24 with $T = 5$ s) and 180 s (36 with $T = 5$ s). It can be seen that, as expected, increasing the prediction horizon leads to a reduction in the battery energy consumption for Case II. Compared with the first two cases, Case III exhibits the highest energy consumptions. Moreover, unlike Cases I and II, Case III does not show a monotonic decrease—mainly because the results are affected by the uncertainty in the vehicle speed preview—in the battery energy consumption as the prediction horizon increases; however, the minimum battery energy consumption is observed again at $N = 180$.

For the first and third cases with $T = 1$ s, Fig. 8(b) shows that the average computation time per time step of the S-MPC increases significantly as the prediction horizon becomes longer. The S-MPC with a long horizon (e.g., $N > 120$) is computationally expensive with average computation time exceeding the sampling time $T = 1$ s. This indicates that the real-time implementation of the S-MPC over a long prediction

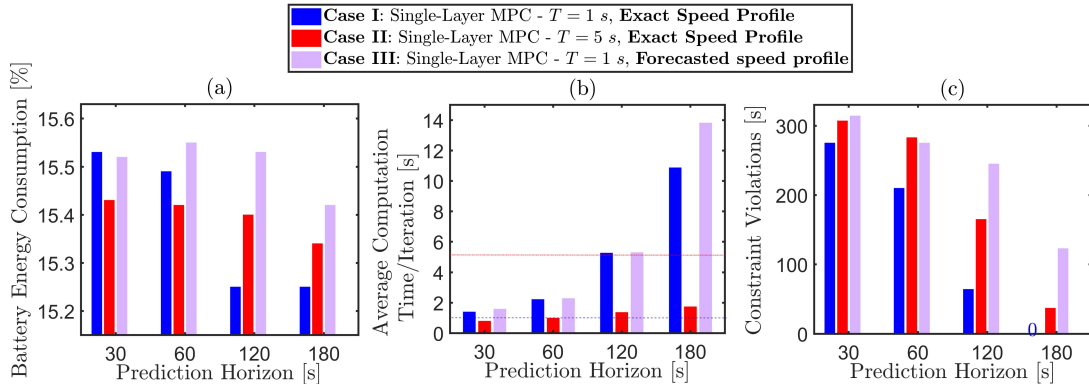


Fig. 8. Sensitivity of S-MPC performance to vehicle speed preview accuracy and sampling rate for different prediction horizons and $T_{\text{bat}}(0) = 35^\circ\text{C}$. (a) Battery energy consumption. (b) Average computation time per iteration. (c) Battery temperature constraint violations.

horizon will require significant algorithmic and computational simplifications. On the other hand, with $T = 5$ s (Case II), the average computation time of S-MPC is much lower.

Fig. 8(c) compares the violation of the battery temperature limit $T_{\text{bat}}^{\text{UL}}$ in terms of the time period during which the battery temperature has stayed over $T_{\text{bat}}^{\text{UL}}$. While increasing the prediction horizon decreases battery temperature constraint violation in all three cases, it can be seen that when the sampling time is increased to 5 s (Case II), the battery temperature constraint violation increases. Furthermore, when S-MPC is implemented with the forecast vehicle speed and not the exact vehicle speed and with $T = 1$ s (Case III), Fig. 8(c) shows that battery temperature constraint violations increase for all choices of the prediction horizon.

Remark 5: Fig. 8(c) shows the time period during which the battery temperature exceeds the constraint, reflecting the performance of the MPC-based BTM in enforcing the battery temperature constraint. To measure this violation intensity, which is of importance, the normalized constraint violation intensity (NCVI) index defined as follows is introduced:

$$\text{NCVI} = \frac{\int_{t_0}^{t_f} f_{\text{NCVI}}(t) dt}{t_f - t_0} \quad (16)$$

where t_0 and t_f denote the initial and end times of the trip, respectively. The function f_{NCVI} is defined as

$$f_{\text{NCVI}}(t) = \begin{cases} 0, & \text{if } T_{\text{bat}} \leq T_{\text{bat}}^{\text{UL}} \\ T_{\text{bat}} - T_{\text{bat}}^{\text{UL}}, & \text{if } T_{\text{bat}} > T_{\text{bat}}^{\text{UL}} \end{cases} \quad (17)$$

For Case I shown in Fig. 8, the NCVI index is shown in Fig. 9. By comparing the trend in Fig. 9 with that of Fig. 8(c), one can see that the intensity of the battery temperature constraint violation has a direct relationship with the period of the violation. When the MPC has a shorter lead time (prediction horizon), the intensity of the constraint violation is larger as it takes a longer time to recover while the traction power and BTM power consumption are both at their peaks.

In conclusion, the benefits of S-MPC with a long prediction horizon for BTM are sensitive to the accuracy and the update rate of the vehicle speed preview. Fig. 6 highlights the complexity and challenges of implementing S-MPC over long horizons as well. Besides the BTM energy consumption and

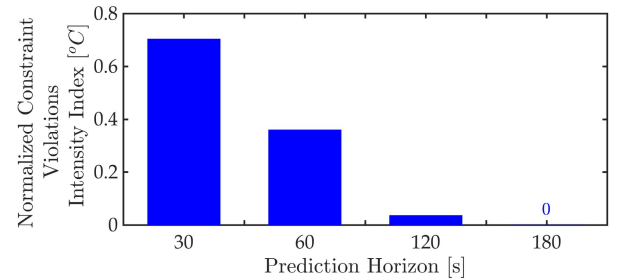


Fig. 9. NCVI index for Case I in Fig. 8.

T_{bat} constraint violations indices, as shown in Fig. 6, the computation time and vehicle speed preview accuracy affect the design and implementation of S-MPC. Based on the results in Fig. 8, the S-MPC with long prediction horizon cannot address all the BTM design challenges and requirements, mainly due to its lack of robustness against the uncertainty in the vehicle speed preview and high computational demands.

IV. H-MPC

In order to leverage the energy-saving potential of the long-horizon vehicle speed forecasts and reduce the computation time of the S-MPC, we propose an H-MPC with scheduling and piloting layers, as shown in Fig. 10. The scheduling layer has a relatively long horizon (H_s) and a large sampling period T_s . The piloting layer has a short prediction horizon H_p with a sampling period $T_p < T_s$, which is an integer fraction of T_s . In this article, we assume that the vehicle speed can be accurately forecast over the short horizon H_p . Over the long horizon H_s and beyond H_p horizon, the vehicle speed prediction is based on the average traffic flow data that are updated every T_s s as the traffic flow changes downstream.

A. Scheduling Layer MPC With a Long Horizon

The scheduling layer MPC is based on the following optimization problem formulation:

$$\begin{aligned} \min_{\hat{Q}(\cdot|k_s), \zeta(\cdot|k_s)} & \sum_{i=0}^{H_s} P_{\text{BTM}}(i|k_s) + \gamma_2 \zeta(i|k_s) \\ \text{s.t. } & T_{\text{bat}}(i+1|k_s) = f_{T_{\text{bat},s}}(i|k_s), \quad i = 0:H_s \\ & \text{SOC}(i+1|k_s) = f_{\text{SOC},s}(i|k_s), \quad i = 0:H_s \end{aligned}$$

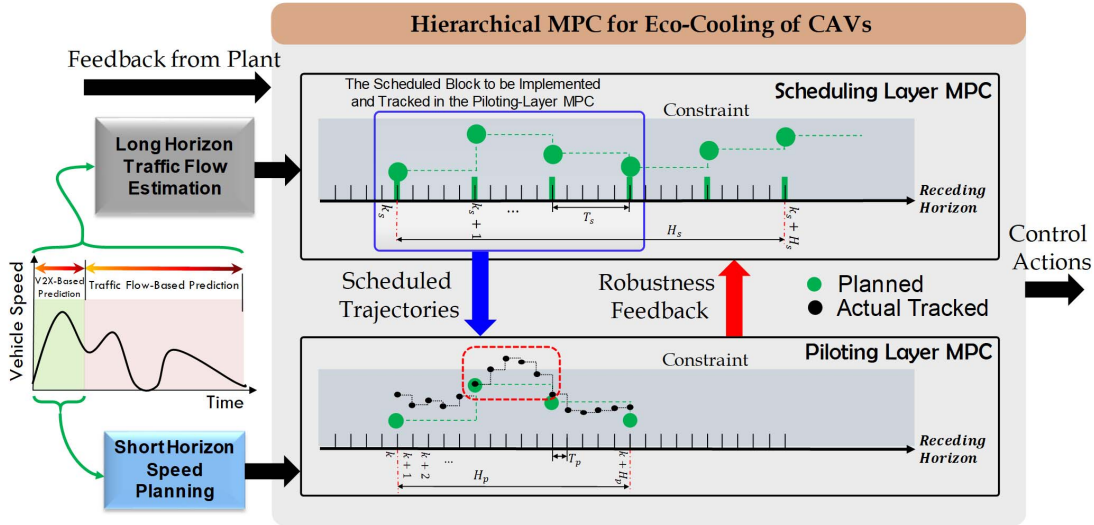


Fig. 10. Schematic of the H-MPC for eco-cooling of CAVs.

$$\begin{aligned}
 T_{\text{bat}}^{\text{LL}} &\leq T_{\text{bat}}(i|k_s) \leq T_{\text{bat}}^{\text{UL}} + \zeta(i|k_s), \quad i = 0:H_s \\
 0.3 &\leq \text{SOC}(i|k_s) \leq 0.9, \quad i = 0:H_s \\
 -\dot{Q}_{\text{max}} &\leq \dot{Q}(i|k_s) \leq 0, \quad i = 0:H_s - 1 \\
 0 &\leq \zeta(i|k_s), \quad i = 0:H_s - 1 \\
 T_{\text{bat}}(0|k_s) &= T_{\text{bat}}(k_s), \quad \text{SOC}(0|k_s) = \text{SOC}(k_s). \quad (18)
 \end{aligned}$$

The scheduling layer MPC optimizes \dot{Q} over the long horizon H_s , and the solution (\dot{Q}^*) is used to determine the desired trajectories of the battery temperature (T_{bat}^*) and the state-of-charge (SOC^*) for the piloting layer. The sequence of control input \dot{Q}^* is updated every T_s s and is indexed by k_s . In addition, $f_{T_{\text{bat}},s}$ and $f_{\text{SOC},s}$ are the discretized nonlinear dynamics of SOC and T_{bat} calculated according to (11) and (12) with larger sampling time of T_s . This results in a reduced computational load, as shown in Fig 8(b). Note that the structure of the scheduling layer MPC is similar to the S-MPC in (13) but with a slower sampling rate. Similar to the S-MPC, an slack optimization variable (ζ) is introduced to soften $T_{\text{bat}}^{\text{UL}}$ with constant $\gamma_2 = 10^7$ in the stage cost.

B. Piloting Layer MPC With a Short Horizon

The planned trajectories, T_{bat}^* and SOC^* , computed by the scheduling layer are passed on to the piloting layer, where these values are used by a short-horizon MPC for tracking. Within each update interval of the scheduling layer MPC, the output of the short-horizon MPC is updated T_s/T_p times. The “block” of the scheduled values that need to be passed on to the piloting layer depends on the piloting layer prediction horizon (H_p). Following a similar approach to [15] for transmitting the planned states from the scheduling layer controller to the lower layer piloting controller, the scheduled T_{bat}^* and SOC^* are passed on as piecewise constant functions: $T_{\text{bat}}^*(t|k)$ and $\text{SOC}^*(t|k)$, where the integer k denotes the time step of the piloting layer with a faster update rate. Fig. 10 shows the communication process between the two layers of the H-MPC.

The short-horizon MPC of the piloting layer for tracking the scheduled T_{bat}^* and SOC^* references is based on the solution

of the following optimization problem:

$$\begin{aligned}
 \min_{\dot{Q}(\cdot|k)} &\sum_{j=0}^{H_p} \left\{ \left((T_{\text{bat}}(j|k) - T_{\text{bat}}^*(j|k))^2 \right. \right. \\
 &\quad \left. \left. + w_1 (\text{SOC}(j|k) - \text{SOC}^*(j|k))^2 \right\} \\
 \text{s.t. } &T_{\text{bat}}(j+1|k) = f_{T_{\text{bat}}}(j|k), \quad j = 0:H_p \\
 &\text{SOC}(j+1|k) = f_{\text{SOC}}(j|k), \quad j = 0:H_p \\
 &-\dot{Q}_{\text{max}} \leq \dot{Q}(j|k) \leq 0, \quad j = 0:H_p - 1 \\
 &T_{\text{bat}}(0|k) = T_{\text{bat}}(k), \quad \text{SOC}(0|k) = \text{SOC}(k) \quad (19)
 \end{aligned}$$

where $w_1 = 0.2$ is a constant weighting factor. When performing optimization in the piloting layer, we assume that an accurate preview of vehicle speed and the demanded traction power are available over the short horizon. Moreover, the constraints on the battery temperature and SOC are not considered, as the scheduling layer MPC enforces these constraints over a long horizon. Not including these constraints reduces the computation time of the piloting layer optimization problem and avoids the infeasibility of the short-horizon MPC, as the scheduled trajectories based on the average traffic speed may be infeasible at the piloting layer where the actual driving speed is incorporated. For the EV BTM case study, we consider $T_s = 5$ s and $T_p = 1$ s.

Fig. 11 compares the battery energy consumption and the temperature constraint violation of the H-MPC with $H_s = 36$ (180 s) and $H_p = 30$ (30 s) and of the S-MPC from Section III with $N = 180$ (180 s) for different values of sampling rate and vehicle speed preview accuracy. With the same forecast vehicle speed used for the S-MPC and H-MPC, and with the same sampling time ($T_s = T = 5$ s), H-MPC results in less frequent constraint violation (by 55%), while its energy consumption is slightly higher (0.4%) than the S-MPC.

The reduced battery temperature constraint violations with the H-MPC compared with the S-MPC can be explained in reference to the BTM operation in adjusting the battery temperature, as shown in Figs. 12 and 13. Fig. 12 shows

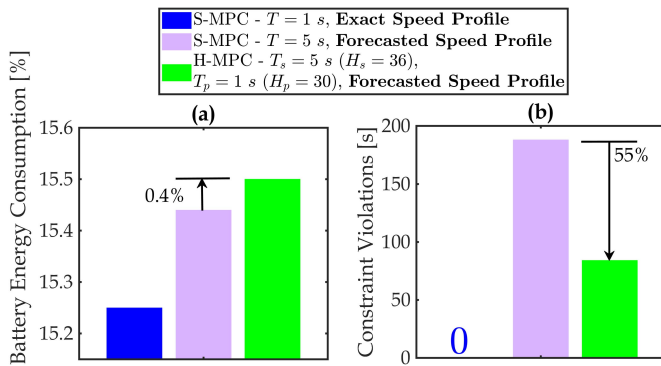


Fig. 11. Performance of the baseline H-MPC compared with S-MPC with a different vehicle speed preview information accuracy. (a) Battery energy consumption. (b) Battery temperature constraint violation. The prediction horizon of the S-MPC is $N = 180$, while the prediction horizons of the H-MPC are $H_s = 36$ (180 s) in the scheduling layer, and 30 (30 s) in the piloting layer. $T_{\text{bat}}(0) = 35$ °C.

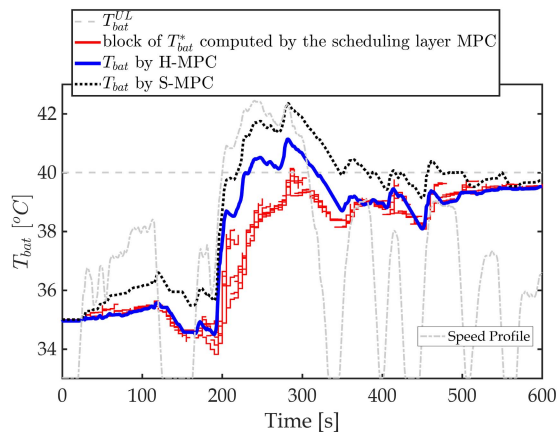


Fig. 12. Planned (predicted) and actual battery temperatures based on the estimated long-horizon forecast vehicle speed. (a) H-MPC with $H_s = 36$, $H_p = 30$, $T_s = 5$ s, and $T_p = 1$ s. (b) S-MPC with $N = 36$ and $T = 5$ s. For both cases, $T_{\text{bat}}(0) = 35$ °C.

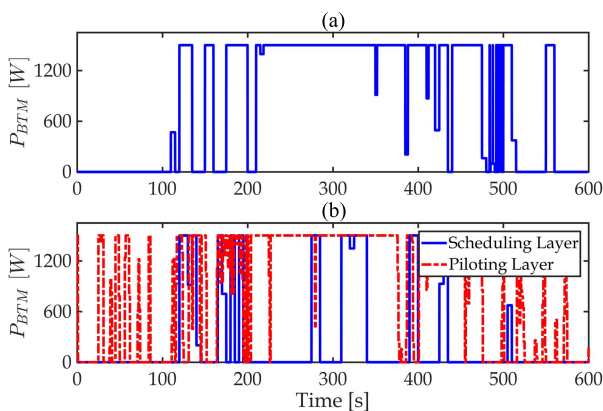


Fig. 13. Time histories of the control input ($P_{\text{BTM}} = a_c \dot{Q}$) with the S-MPC and H-MPC at scheduling and piloting layers. (a) S-MPC with $N = 36$ and $T = 5$ s. (b) H-MPC with $H_s = 36$, $H_p = 30$, $T_s = 5$ s, and $T_p = 1$ s. For both cases, $T_{\text{bat}}(0) = 35$ °C.

that the “block” of planned temperature trajectories (shown in red) to be tracked by the piloting layer MPC over the short horizon satisfies the temperature constraint. Moreover, since the piloting layer MPC tracks these trajectories, the actual

battery temperature (shown in dark blue) will remain close to the block of scheduled T_{bat}^* . The error in tracking the scheduled trajectories by the piloting layer MPC is mainly due to the mismatch between the long-term forecast vehicle speed and the actual vehicle speed, which makes the ideal tracking of the planned trajectories infeasible for the piloting layer controller. On the other hand, when the S-MPC calculates and applies the optimal \dot{Q}^* , the actual T_{bat} (shown in dotted black) is different than the predicted one, where the latter is calculated according to the model ($f_{T_{\text{bat}}}$) used in S-MPC after finding the optimal control action. The S-MPC mechanism to compensate this deviation is to further reduce the planned battery temperature in the next time steps so that the actual temperature also decreases. However, Fig. 12 shows that once the actual battery temperature rises, decreasing the planned thermal trajectory cannot avoid the constraint violation, as the slow thermal dynamics requires cooling actions in advance to avoid violation of $T_{\text{bat}}^{\text{UL}}$.

The H-MPC adjusts the control commands at the piloting layer [see Fig. 13(b)] by tracking the planned trajectory, while it has access to more accurate vehicle speed prediction over the short horizon. Thus, thanks to the piloting layer of H-MPC for enforcing the tracking of the planned trajectories and utilizing the short horizon accurate speed prediction, the sensitivity of the battery thermal response to vehicle speed forecast uncertainty over the long horizon is reduced. Note that the first element of the computed optimal control sequence of S-MPC ($P_{\text{BTM}}^*(k)$) and H-MPC at the scheduling ($P_{\text{BTM}}^*(k_s)$) and piloting ($P_{\text{BTM}}^*(k)$) layers are plotted in Fig. 13.

Furthermore, the H-MPC framework can be extended by additional algorithms to monitor the deviation in the planned and actual battery temperature trajectories between the scheduling and piloting layers, primarily caused by the uncertainty in the long-term vehicle speed prediction. Upon the detection of these deviations in the BTM performance, the constraint sets in the scheduling layer can be tightened for reducing the likelihood of battery temperature constraint violation. This mitigating strategy will be discussed in Section V.

V. ROBUST H-MPC FOR ECO-COOLING

In this section, first, a “passive” CT algorithm is proposed and added to the structure of the H-MPC at the scheduling layer to tighten the battery temperature constraint after the violation of the constraint is detected. Second, a novel “proactive” CT algorithm is developed, which, unlike the passive CT approach, proactively determines the constraint violation over the short prediction horizon of the piloting layer MPC. In this approach, the piloting-layer MPC shares the constraint violation predictions with the scheduling layer MPC, and the scheduling layer MPC tightens the constraint before the violation occurs. The passive- and proactive-CT algorithms are operating according to internal feedback from the piloting layer MPC to the scheduling layer MPC. This feedback is highlighted in Fig. 10 as the robustness feedback.

A. Robust H-MPC With Passive CT

A “passive” CT (passive-CT) algorithm is added to the structure of the H-MPC to reduce the battery temperature

limit violation. The passive-CT algorithm takes into account the violation of the battery temperature limits after it occurs, and it monitors the difference between T_{bat} and $T_{\text{bat}}^{\text{UL}}$. The addition of the passive-CT algorithm introduces an extra slack optimization variable ϵ , which modifies the upper temperature bound at the scheduling layer to reduce temperature limit violations at the piloting layer. For this purpose, the scheduling layer cost function in (18) is modified as follows:

$$\min_{\dot{Q}(i|k_s), \epsilon(i|k_s)} \sum_{i=0}^{H_s} P_{\text{BTM}}(i|k_s) + \gamma (\delta(T_{\text{bat}}, T_{\text{bat}}^{\text{UL}}) - \epsilon(i|k_s))^2 \quad (20)$$

where γ is a weighting factor to adjust the controller effort for tightening $T_{\text{bat}}^{\text{UL}}$. The scheduling layer MPC is subject to all the constraints listed in (18), except the one on $T_{\text{bat}}(i|k_s)$, which is modified to

$$\begin{aligned} T_{\text{bat}}(i|k_s) &\leq T_{\text{bat}}^{\text{UL}} - \epsilon(i|k_s), \quad i = 0:H_s \\ 0 &\leq \epsilon(i|k_s), \quad i = 0:H_s - 1. \end{aligned} \quad (21)$$

The function $\delta(T_{\text{bat}}, T_{\text{bat}}^*)$ in (20) is defined as follows:

$$\delta(T_{\text{bat}}, T_{\text{bat}}^{\text{UL}}) = \begin{cases} 0, & \text{if } T_{\text{bat}} < T_{\text{bat}}^{\text{UL}} \\ T_{\text{bat}} - T_{\text{bat}}^{\text{UL}}, & \text{if } T_{\text{bat}} \geq T_{\text{bat}}^{\text{UL}}. \end{cases} \quad (22)$$

B. Robust H-MPC With Proactive CT

The proactive-CT approach exploits the fact that the piloting layer has access to more accurate vehicle speed prediction and model of the dynamics due to a higher sampling rate than the scheduling layer. Hence, it can predict the deviation in the temperature tracking compared with the planned set-point over the short horizon. Then, the constraints of the scheduling layer MPC at next time instant can be proactively tightened to accommodate such predicted deviations.

At the piloting layer, first, the sequence of optimal control inputs over the short horizon ($\dot{\mathbf{Q}} = [\dot{Q}(j|k), \dot{Q}(j+1|k), \dots, \dot{Q}(j+H_p|k)]^T$) is computed once the optimization problem (19) is solved at time step k . Next, based on $\dot{\mathbf{Q}}$ and the prediction model $f_{T_{\text{bat}}}$, and according to the accurate traction power demand available over the short horizon H_p , the sequence of future battery temperature \hat{T}_{bat} states is calculated ($\hat{\mathbf{T}}_{\text{bat}} = [\hat{T}_{\text{bat}}(j+1|k), \hat{T}_{\text{bat}}(j+2|k), \dots, \hat{T}_{\text{bat}}(j+H_p+1|k)]^T$). The error (\mathbf{e}) between $\hat{\mathbf{T}}_{\text{bat}}$ and the planned trajectory by the scheduling layer MPC ($\mathbf{T}_{\text{bat}}^*$) is then predicted as $\mathbf{e} = \hat{\mathbf{T}}_{\text{bat}} - \mathbf{T}_{\text{bat}}^*$, where $\mathbf{T}_{\text{bat}}^*$ is upsampled to the rate of short horizon MPC. The maximum of \mathbf{e} is used as the robustness feedback [$e_{\text{max}} = \max(\mathbf{e})$] from the piloting layer to the scheduling layer for the next iteration, e.g., $k_s + 1$, thereby enabling the long-horizon scheduling MPC to proactively tighten the temperature constraint based on the prediction of the constraint violation made at the piloting layer. This process is illustrated and summarized in Fig. 14.

For the H-MPC with proactive-CT, the scheduling layer MPC (18) is subject to all the constraints listed in (18), except the one on $T_{\text{bat}}(i|k_s)$, which is now modified to

$$T_{\text{bat}}(i|k_s) \leq T_{\text{bat}}^{\text{UL}} - e_{\text{max}}(k_s - 1) + \zeta(i|k_s) \quad (23)$$

where $i = 0, \dots, H_s$. Note that e_{max} in (23) is computed from the previous time instant $k_s - 1$.

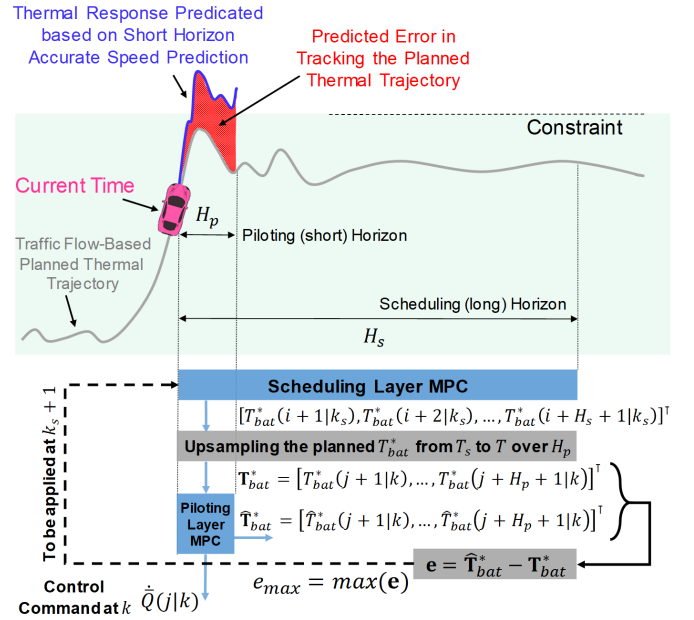


Fig. 14. Concept and process of estimating the deviation in the thermal response over the piloting-layer short horizon (H_p) for incorporation in H-MPC with proactive-CT.

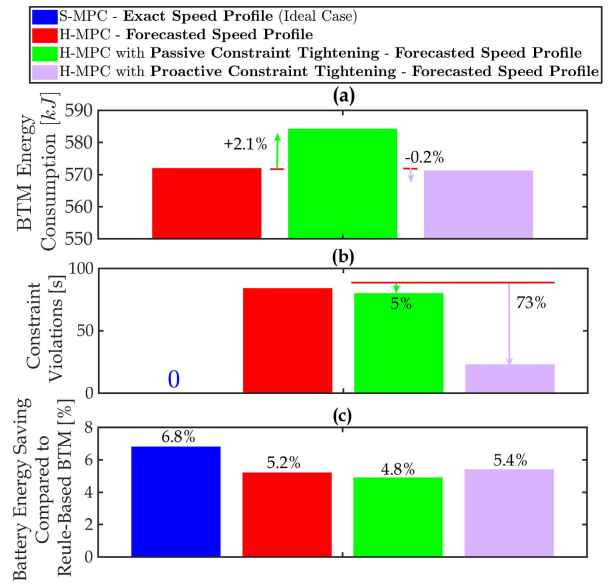


Fig. 15. Performance of the proposed robust H-MPCs compared with baseline H-MPC and S-MPC for $T_{\text{bat}}(0) = 35$ °C over UDDS. (a) Battery temperature. (b) BTM energy consumption. (c) Constraint violation. (d) Battery energy saving compared with the rule-based BTM controller.

VI. PERFORMANCE OF THE ROBUST H-MPC

The overall performance of the baseline H-MPC and the proposed H-MPCs with passive- and proactive-CT algorithms from Section V are now compared, and the results are shown in Fig. 15 with $T_{\text{bat}}(0) = 35$ °C. The performance of the S-MPC with $N = 180$, $T = 1$ s and exact knowledge of the vehicle speed profile is also plotted in Fig. 15 as the ideal case. Fig. 15(b) shows that the proposed robust H-MPCs are reducing the battery temperature constraint violations

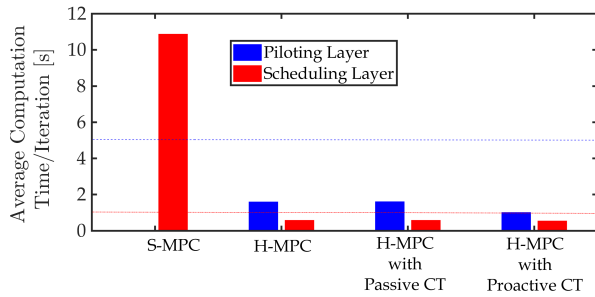


Fig. 16. Average computation time per iteration for different MPCs evaluated for BTM.

compared with the baseline H-MPC. While the proactive-CT strategy is able to reduce the constraint violations significantly by 73%, it is observed that the passive-CT algorithm reduces the $T_{\text{bat}}^{\text{UL}}$ violations only by 5%.

Fig. 15(a) shows the battery energy consumed for BTM, and Fig. 15(c) depicts the achieved battery energy saving using MPC-based BTM solutions compared with the rule-based controller. It is noted that while the passive-CT algorithm has the highest BTM energy consumption [see Fig. 15(a)] and the lowest overall battery energy saving [see Fig. 15(c)], it fails to reduce the constraint violations effectively. The H-MPC with proactive-CT, on the other hand, outperforms the H-MPC with passive-CT in all of the performance indices. The H-MPC with proactive-CT reacts to the potential temperature violations in advance, thereby reducing the BTM energy consumption after the violation occurs. With an approximate knowledge of the future driving cycle, the H-MPC with proactive-CT shows that how we can capitalize on the vehicle speed preview knowledge to achieve a robust eco-cooling, without making the controller too conservative.

The computation times of different MPCs for BTM are compared in Fig. 16 with $N = 180$, $H_s = 36$, $H_p = 30$, $T = 1$ s, $T_s = 5$ s, and $T_p = 1$ s. Compared with the S-MPC, H-MPCs show significantly lower computation demands at both layers because of the larger sampling time used at the scheduling layer and the nonredundant constraint enforcement. In addition, Fig. 16 shows that H-MPC with proactive-CT has the lowest computation demands. This could be due to better handling of constraint violations by the proactive-CT algorithm, which results in less frequent optimization iteration with active constraints.

VII. CONCLUSION

A robust H-MPC-based battery thermal and energy management strategy was developed in this article to improve energy efficiency and extend the driving range of connected and automated battery EVs.

- 1) First, given the relatively slow thermal dynamics of the battery, the importance of long-horizon optimization for BTM to achieve energy efficiency benefits was shown. The long-horizon BTM optimization allows for eco-cooling of the battery by shifting the major BTM system power demand to low/moderate traction power demand periods, thereby reducing the BTM load on the battery during high-acceleration periods of the vehicle

driving cycle. It was shown that the S-MPC is highly sensitive to the accuracy and update rate of the future vehicle speed predictions. In addition, the S-MPC with a long prediction horizon was shown to be computationally demanding.

- 2) Second, in order to exploit the energy-saving potential of the long-horizon MPC-based BTM and reduce the computation complexity of the S-MPC with a long horizon, we proposed an H-MPC for battery thermal and energy management.
- 3) Third, to achieve robust eco-cooling, we developed and evaluated two constraint tightening algorithms integrated within the H-MPC framework. We showed that since the H-MPC is able to utilize the future vehicle speed predictions with different accuracies over different prediction horizons at each layer, the deviation of the actual battery temperature response from the planned trajectories can be estimated over a short horizon. The resulting estimate was then used to proactively tighten constraints in the scheduling layer, leading to a more robust performance with fewer constraint violations, while consuming less battery energy for BTM.

The simulation results over UDSS and under the vehicle speed forecast uncertainty showed that the H-MPC with proactive-CT regulates the battery temperature within the prescribed operating range with minimum constraint violations while consuming, on average, 25% less energy for BTM compared with the conventional strategy that tracks a constant temperature set-point. This translates into 5.4% energy savings at the vehicle level over the conventional strategy. The proposed H-MPC approach may have other use for control of autonomous systems beyond the system considered here.

While the performance, robustness, and effectiveness of the proposed eco-cooling strategy were studied and confirmed over UDSS, a comprehensive study of evaluating the MPC-based BTM performance for electrified vehicles over different representative driving cycles, including real-work urban cycles, is left as the topic for future research. Another possible direction for future works could be the study of opportunities to use friction brakes to shift the thermal load on the battery.

REFERENCES

- [1] A. Sciarretta, G. De Nunzio, and L. Leon Ojeda, "Optimal ecodriving control: Energy-efficient driving of road vehicles as an optimal control problem," *IEEE Control Syst. Mag.*, vol. 35, no. 5, pp. 71–90, Oct. 2015.
- [2] J. Guanetti, Y. Kim, and F. Borrelli, "Control of connected and automated vehicles: State of the art and future challenges," *Annu. Rev. Control*, vol. 45, pp. 18–40, 2018.
- [3] A. Vahidi and A. Sciarretta, "Energy saving potentials of connected and automated vehicles," *Transp. Res. C, Emerg. Technol.*, vol. 95, pp. 822–843, Oct. 2018.
- [4] M. R. Amini, H. Wang, X. Gong, D. Liao-McPherson, I. Kolmanovsky, and J. Sun, "Cabin and battery thermal management of connected and automated HEVs for improved energy efficiency using hierarchical model predictive control," *IEEE Trans. Control Syst. Technol.*, to be published, doi: [10.1109/TCST.2019.2923792](https://doi.org/10.1109/TCST.2019.2923792).
- [5] M. R. Amini, X. Gong, Y. Feng, H. Wang, I. Kolmanovsky, and J. Sun, "Sequential optimization of speed, thermal load, and power split in connected HEVs," in *Proc. Amer. Control Conf. (ACC)*, Philadelphia, PA, USA, Jul. 2019, pp. 4614–4620.

- [6] S. Bauer, A. Suchanek, and F. Puente León, "Thermal and energy battery management optimization in electric vehicles using Pontryagin's maximum principle," *J. Power Sources*, vol. 246, pp. 808–818, Jan. 2014.
- [7] J. Neubauer and E. Wood, "Thru-life impacts of driver aggression, climate, cabin thermal management, and battery thermal management on battery electric vehicle utility," *J. Power Sources*, vol. 259, pp. 262–275, Aug. 2014.
- [8] E. Kim, K. G. Shin, and J. Lee, "Real-time battery thermal management for electric vehicles," in *Proc. ACM/IEEE Int. Conf. Cyber-Phys. Syst. (ICCP)*, Berlin, Germany, Apr. 2014, pp. 72–83.
- [9] Y. Masoudi, A. Mozaffari, and N. Azad, "Battery thermal management of electric vehicles: An optimal control approach," in *Proc. ASME Dyn. Syst. Control Conf.*, Columbus, OH, USA, 2015, Art. no. V001T13A003.
- [10] Z. Yang, Y. Feng, X. Gong, D. Zhao, and J. Sun, "Eco-trajectory planning with consideration of queue along congested corridor for hybrid electric vehicles," *Transp. Res. Rec., J. Transp. Res. Board*, vol. 2673, no. 9, pp. 277–286, May 2019.
- [11] D. Moser, H. Waschl, R. Schmied, H. Efendic, and L. del Re, "Short term prediction of a vehicle's velocity trajectory using ITS," *SAE Int. J. Passenger Cars-Electron. Electr. Syst.*, vol. 8, no. 2, pp. 364–370, Apr. 2015.
- [12] M. R. Amini, J. Sun, and I. Kolmanovsky, "Two-layer model predictive battery thermal and energy management optimization for connected and automated electric vehicles," in *Proc. IEEE Conf. Decis. Control (CDC)*, Miami Beach, FL, USA, Dec. 2018, pp. 6976–6981.
- [13] S. Raimondi Cominesi, M. Farina, L. Giulioni, B. Picasso, and R. Scattolini, "A two-layer stochastic model predictive control scheme for microgrids," *IEEE Trans. Control Syst. Technol.*, vol. 26, no. 1, pp. 1–13, Jan. 2018.
- [14] J. P. Koeln and A. G. Alleyne, "Robust hierarchical model predictive control of graph-based power flow systems," *Automatica*, vol. 96, pp. 127–133, Oct. 2018.
- [15] A. Lefort, R. Bourdais, G. Ansanay-Alex, and H. Guéguen, "Hierarchical control method applied to energy management of a residential house," *Energy Buildings*, vol. 64, pp. 53–61, Sep. 2013.
- [16] H. Wang, I. Kolmanovsky, M. R. Amini, and J. Sun, "Model predictive climate control of connected and automated vehicles for improved energy efficiency," in *Proc. Annu. Amer. Control Conf. (ACC)*, Milwaukee, WI, USA, Jun. 2011, pp. 828–833.
- [17] Q. Wang, B. Jiang, B. Li, and Y. Yan, "A critical review of thermal management models and solutions of lithium-ion batteries for the development of pure electric vehicles," *Renew. Sustain. Energy Rev.*, vol. 64, pp. 106–128, Oct. 2016.
- [18] *SAE Surface Vehicle Information Report*. Warrendale, PA, USA: SAE International, 2016.
- [19] S. Halbach, P. Sharer, S. Pagerit, A. Rousseau, and C. Folkerts, "Model architecture, methods, and interfaces for efficient math-based design and simulation of automotive control systems," 2010, SAE Tech. Paper 2010-01-0241, 2010.
- [20] M. Zolot, A. Pesaran, and M. Mihalic, "Thermal evaluation of Toyota prius battery pack," SAE Tech. Paper 2002-01-1962, 2002.
- [21] J. Lofberg, "YALMIP: A toolbox for modeling and optimization in MATLAB," in *Proc. IEEE Int. Conf. Robot. Autom.*, New Orleans, LA, USA, Sep. 2004, pp. 284–289.
- [22] A. Wächter and L. T. Biegler, "On the implementation of an interior-point filter line-search algorithm for large-scale nonlinear programming," *Math. Program.*, vol. 106, no. 1, pp. 25–57, Apr. 2005.
- [23] N. Murgovski, L. Johannesson, and J. Sjöberg, "Convex modeling of energy buffers in power control applications," *IFAC Proc. Volumes*, vol. 45, no. 30, pp. 92–99, 2012.
- [24] E. Tate and S. Boyd, "Finding ultimate limits of performance for hybrid electric vehicles," SAE Tech. Paper 2000-01-3099, 2000.
- [25] C. Zhu, F. Lu, H. Zhang, J. Sun, and C. C. Mi, "A real-time battery thermal management strategy for connected and automated hybrid electric vehicles (CAHEVs) based on iterative dynamic programming," *IEEE Trans. Veh. Technol.*, vol. 67, no. 9, pp. 8077–8084, Sep. 2018.
- [26] Q. Hu, M. Amini, H. Wang, I. Kolmanovsky, and J. Sun, "Integrated power and thermal management of connected HEVs via multi-horizon MPC," in *Proc. ACC*, Denver, CO, USA, 2020.
- [27] C. Sun, F. Sun, X. Hu, J. K. Hedrick, and S. Moura, "Integrating traffic velocity data into predictive energy management of plug-in hybrid electric vehicles," in *Proc. Amer. Control Conf. (ACC)*, Chicago, IL, USA, Jul. 2015, pp. 3267–3272.
- [28] J. C. Herrera, D. B. Work, R. Herring, X. J. Ban, Q. Jacobson, and A. M. Bayen, "Evaluation of traffic data obtained via GPS-enabled mobile phones: The mobile century field experiment," *Transp. Res. C, Emerg. Technol.*, vol. 18, no. 4, pp. 568–583, Aug. 2010.



Mohammad Reza Amini received the Ph.D. degree in mechanical engineering from Michigan Technological University, Houghton, MI, USA, in 2017.

He is currently an Assistant Research Scientist with the College of Engineering, University of Michigan, Ann Arbor, MI, USA. His research interests in nonlinear, adaptive, and predictive control theories and their applications to intelligent transportation, automotive, and energy systems.



Ilya Kolmanovsky (Fellow, IEEE) received the Ph.D. degree from the University of Michigan, Ann Arbor, MI, USA, in 1995.

He is currently a Professor with the Department of Aerospace Engineering, University of Michigan. His research interests in control theory for systems with state and control constraints, and in control applications to aerospace and automotive systems.



Jing Sun (Fellow, IEEE) received the Ph.D. degree from the University of Southern California, Los Angeles, CA, USA, in 1989.

She is currently a Professor and the Chair with the Naval Architecture and Marine Engineering Department, University of Michigan, Ann Arbor, MI, USA. Her research interests include modeling, control, and optimization of dynamic systems, with applications to marine and automotive systems.

Dr. Sun is a fellow of the National Academy of Inventors, IFAC, and the Society of Naval Architects and Marine Engineers. She was a recipient of the 2003 IEEE Control System Technology Award.